Microchimica Acta (2020) 187:494
https://doi.org/10.1007/s00604-020-04467-5

ORIGINAL PAPER

Electrochemical biosensor for detection of MON89788 gene fragments with spiny trisoctahedron gold nanocrystal and target DNA recycling amplification

Yuanfeng Peng[1] · Ruiyi Li[2] · Minyi Yu[1] · Xiaowen Yi[1] · Haiyan Zhu[1] · Zaijun Li[1] · Yongqiang Yang[3]

Received: 1 February 2020 / Accepted: 27 July 2020

Abstract

The shape-controlled synthesis of gold nanocrystals via shape induction of hexadecyltrimethylammonium chloride, potassium bromide, and potassium iodide and enantioselective direction of L-cysteine is reported. The resulting gold nanocrystals (STO-Au) offer spiny trisoctahedron nanostructures with good monodispersity and enhanced exposed high-index facets and high catalytic activity. Construction of the electrochemical sensing platform for MON89788 gene involves the modification of STO-Au, thionine (Thi), and labeled bipedal DNA probe 1 or 2 (P1 or P2) for target DNA–induced recycling amplification. In the detection, two surface DNA probes were immobilized on gold electrode via the Au-S bond. Then, hairpin DNA 1 (H1), Thi-STO-Au-P1, and Thi-STO-Au-P2 self-assemble into two-dimensional DNA nanopores (DNPs) on the electrode surface. Target DNA hybridizes with hairpin DNA 2 (H2) to open hairpin structure of H2. The opened H2 binds with H1 in the DNPs to release Thi-STO-Au-P1, Thi-STO-Au-P2, and target DNA by toehold-mediated strand-displacement. The utilization of target DNA–induced recycling allows one target DNA to release 2N STO-Au-labeled DNA strands, promoting significant signal amplification. The detection signal is further enhanced by the catalyzed redox reaction of Thi with STO-Au. The differential pulse voltammetric signal, best measured at − 0.18 V vs. Ag/AgCl, decreases linearly with increasing concentration of MON89788 in the range 0.02–8 × 10^4 fM, and the detection limit is 0.0048 fM ($S/N = 3$). The proposed method was successfully applied for electrochemical detection of MON89788 gene fragments in the PCR products from genetically modified soybean.

Keywords Nanomaterials · Transgenic soybean · Voltammetric method · Enzyme-free amplification · Regeneration-free biosensor

Introduction

DNA detection has been widely applied in disease diagnosis [1], food safety [2], biological identification [3], and archeology [4]. The main techniques for the detection of DNA are fluorescence [5], polymerase chain reaction (PCR) [6], surface-enhanced Raman spectroscopy (SERS) [7], colorimetric method [8], and electrochemical sensor [9]. The fluorescent method offers high sensitivity and selectivity, but it often suffers from background fluorescence interference from biomacromolecules. The PCR is one classical quantitative method for the detection of DNA, but it requires complex sample pretreatment, expensive equipment, and skilled operator. The SERS has high sensitivity, but the instability of detection signal limits its applications. The colorimetric method is rapid, inexpensive, and user-friendly. However, its sensitivity is much lower than that of fluorescence and SERS.

Electronic supplementary material The online version of this article (https://doi.org/10.1007/s00604-020-04467-5) contains supplementary material, which is available to authorized users.

✉ Zaijun Li
zaijunli@jiangnan.edu.cn

✉ Yongqiang Yang
yqyang@wxtjy.com

[1] School of Chemical and Material Engineering, Jiangnan University, Wuxi 214122, China

[2] Lihu Road 1800, Wuxi 214122, Jiangsu, China

[3] National Graphene Product Quality Supervision and Inspection Center, Jiangsu Province Special Equipment Safety Supervision and Inspection Institute Branch, Wuxi 214071, China

Published online: 10 August 2020

Electrochemical biosensor has attracted more attention because of its high sensitivity, simple operation, and low-cost [10]. Numerous investigations have examined various nanomaterials as the electrochemical DNA biosensors to improve the analytical performance, such as silver [11], gold [12], palladium [13], platinum [14], graphene, and titanium dioxide [15]. Gold nanomaterial is the most frequently used electrochemical sensing material due to its facile synthesis, easy surface modification, special catalytic ability, and biocompatibility [16, 17].

Great effort has been devoted to synthesis of gold nanomaterials to increase the surface area, electrical conductivity, and exposure of high-index facets [18]. Large surface brings high exposure of gold atoms, improving the catalytic activity. Taj and co-workers reported the synthesis of ultrasmall gold augmented graphene via the reduction of $HAuCl_4$ using *Caryota mitis* extract as the reducing agent [19]. The resulting gold nanoparticles have the particle size of 2–8 and were successfully applied in the electrochemical detection of uric acid as low as 30 nM. Qin and co-workers developed hollow gold nanoparticles via the reduction of $HAuCl_4$ and $AgNO_3$ with ascorbic acid [20]. The resulted gold nanocrystal displays a hydrangea-like hollow structure. It has been used as the catalyst with a high SERS activity to monitor the reduction reaction. However, the smaller the particle size is, the larger the interface resistance. As a result, small or hollow gold nanomaterial often gives a relatively low electrical conductivity. The researches have demonstrated that the construction of core-shell structure and particle clusters is an effective approach to improve the electrical conductivity of gold nanoparticles [21]. Our group reported a palladium@gold nanoalloy-graphene multiple aerogel [22]. In the nanoalloy, palladium nanocube as the core enhances the electrical conductivity, and gold nanoparticles as the shell improve the catalytic activity. Chuang and co-workers reported the synthesis of gold nanodandelions by growth of gold seeds in the presence of gelatin [23]. Owing to high density of atomic steps, ledges, kinks, and dangling bonds, the high-index facets of gold nanocrystal often give a much better catalytic activity compared with the low-index facets [24]. However, high-index facets of gold nanocrystal are rapidly enclosed by low-index facets during the crystal growth process. To overcome the problem, several polyhedron gold nanocrystals with more exposed high-index facets were developed and used for construction of electrochemical biosensors [25]. However, synthesis of polyhedron gold nanocrystals with excellent catalytic behavior for electrochemical detection of DNA still faces a great challenge up to now.

In this study, we report one strategy for shape-controlled synthesis of gold nanocrystals via shape induction of hexadecyltrimethylammonium chloride, potassium bromide, and potassium iodide and enantioselective direction of L-cysteine. The resulting spiny trisoctahedron gold nanocrystal (STO-Au) shows high catalytic activity. The electrochemical biosensor based on the STO-Au and target DNA recycling amplification achieves high sensitivity, specificity, and repeativity. The proposed method has been successfully applied in electrochemical detection of MON89788 gene fragments in the PCR products from genetically modified soybean.

Experimental

Reagent and materials

Chloroauric acid ($HAuCl_4$), L-cysteine, cetyltrimethylammonium chloride (CTAC), L-ascorbic acid, potassium bromide (KBr), potassium iodide (KI), 6-mercaptohexan-1-ol (MCH), thionine (Thi), and tris(2-carboxyethyl) phosphine hydrochloride (TCEP) were purchased from Sigma-Aldrich Co. LLC (Shanghai, China). All nucleic acids used were synthesized and purified by Sangon Biotech. Co., Ltd. (Shanghai, China). The sequences of all oligonucleotides are listed in Table s1. The DNA stock solution was prepared in Tris/Mg/K buffer containing 20 mM Tris-HCl, 1 mM $MgCl_2$, 1 mM $CaCl_2$, and 5 mM KCl at pH 7.4, and stored at − 20 °C. Other reagents used were purchased from Sinopharm Chemical Reagent Co., Ltd. (Shanghai, China). Phosphate-buffered saline (PBS, pH 7.4, Na_2HPO_4-KH_2PO_4-NaCl-KCl, 0.01 M) was prepared. Ultrapure water (18.2 MΩ cm) purified from Milli-Q purification system was used throughout the experiment.

STO-Au synthesis

The ascorbic acid solution (0.45 mL, 50 mM) was added into 9.55 mL of the $HAuCl_4$ solution containing CTAC, KBr, and KI ($HAuCl_4$: 0.73 mM, CTAC: 15.7 mM, KBr: 5.03 μM, KI: 0.503 μM) under stirring. The solution was incubated at 20 °C for 30 min, followed by centrifugation at 5500 rpm for 1 min and washing three times with ultrapure water. The collected TO-Au was re-dispersed in 3 mL of ultrapure water to obtain a TO-Au stock solution. The above procedure was also used for the preparation of spherical gold nanoparticles (S-Au) unless no addition of CTAC, KBr, and KI.

The $HAuCl_4$ solution (200 μL, 10 mM) was added into 4.86 mL of the mixed TO-Au solution, containing 0.25 mL of the TO-Au stock solution, 15 mM CTAC, 10 μM KBr, 1 μM KI, and 0.1 μM L-cysteine. The ascorbic acid solution (475 μL, 50 mM) was added into the above solution and then incubated at 20 °C for 3 min. It was treated by centrifugation at 5500 rpm for 1 min and washing three times with ultrapure water. The collected STO-Au was re-dispersed in 0.5 mL of ultrapure water to obtain a STO-Au stock solution.

Redox probe preparation

The P1 solution (100 μL, 10 μM) was mixed with an equal volume of TCEP solution (1 mM) and then incubated at 20 °C for 60 min to activate the −SH groups in P1. The STO-Au stock solution (100 μL) was added and then incubated at ambient temperature for 12 h. It was treated by the addition of Thi solution (200 μL, 0.1 mM), incubation in air-bath of 25 °C with vibrating at 250 rpm overnight, centrifugation at 12000 rpm for 10 min, and washing with the Tris-HCl of pH 7.4. The collected Thi-STO-Au-P1 was re-dispersed in the Tris-HCl of pH 7.4. The above procedure was also used for the preparation of Thi-STO-Au-P2 except replacing P1 with P2. The as-prepared Thi-STO-Au-P1 and Thi-STO-Au-P2 were stored at 4 °C until use.

Sensor preparation

The S1 solution (100 μL, 10 μM) was mixed with an equal volume of TCEP solution (1 mM) and then stirred for 60 min to activate S1 [26]. The procedure was also used to activate S2. The activated S1 was mixed with an equal volume of the activated S2. A total of 10 μL of it was dropped on the surface of pre-treated gold electrode (GE, 1 mm in diameter) [27] and then incubated at ambient temperature for overnight. The obtained S1-S2/GE was washed with PBS (pH 7.4, 0.1 M NaCl) to remove free S1 and S2 and then dried with N_2 current. After that, 5 μL of the 6-mercapto-1-hexanol (MCH) solution (1 mM) was dropped on the surface of S1-S2/GE and then incubated at room temperature for 60 min to block unmodified active sites. The obtained MCH/S1-S2/GE was washed with the PBS of pH 7.4, dried with N_2 current, and stored at 4 °C before use in sequence.

DNA extraction and PCR amplification

The soybean sample of 200–500 mg was freeze-dried in liquid nitrogen and then ground to powder. The powder sample was added into the concentrated digestion solution of 10 mL and incubated in water-bath for 48 h at 25 °C, followed by centrifugation at 12000 rpm for 4 min. The collected precipitate was dispersed in 100 mL of the sterilized distilled water. The DNA in the sample solution was immediately extracted according to instructions of Plant Genomic DNA Kit (Sangon Biotech Co., Ltd. Shanghai, China). The concentration of DNA was measured by the absorbance at 260 nm.

The PCR amplification was performed on the Eppendorf Mastercycler Gradient PCR system by using the reported procedure [25]. The obtained PCR products were used as real samples for the electrochemical detection of MON89788 gene fragments. For the detection, the PCR products were quantified, serially diluted, and denatured to single-stranded DNA by incubation at 95 °C for 10 min and immediately frozen in ice for 2 min before use.

MON89788 detection

The annealed H1 (10 μL, 1.0 μM) was mixed with the Thi-STO-Au-P1 (10 μL, 1.0 μM) and Thi-STO-Au-P2 (10 μL, 1.0 μM). A total of 10 μL of it was dropped on the surface of MCH/S1-S2/GE and then incubated at 37 °C for 100 min to form two-dimensional DNA nanoprobes (DNPs). The obtained DNP/MCH/S1-S2/GE was washed with PBS (pH 7.4, 10 mM) and then dried in N_2 current.

The target DNA standard solution or sample solution (5 μL) was mixed with the annealed H2 (5 μL, 2 μM). Then, it was dropped on the surface of DNP/MCH/S1-S2/GE, followed by incubation at 37 °C for 120 min and washing with PBS (pH 7.4, 10 mM). Finally, the modified electrode was immersed in the PBS buffer (pH 7.4, 10 mM) containing 0.1 M NaCl for the cyclic voltammety (CV) and differential pulse voltammetry (DPV) measurements.

Results and discussion

STO-Au synthesis

The synthesis of STO-Au includes two steps (Fig. 1). The first step is to make trisoctahedron gold nanocrystals (TO-Au) via the reduction of $HAuCl_4$ with ascorbic acid in the presence of CTAC, KBr, and KI. Here, CTA^+ was assigned as the soft template. The template provides the micron-scale spaces for reduction of Au^{3+} and growth of gold nanocrystals. As a result, the formed gold nanocrystals have a large particle size of 50–200 nm [28]. Three halogen anions were assigned as the shape inducers to control the growth of gold nanocrystals. Many studies demonstrate that the specie and amount of halogen anion (X^-) may seriously influence the morphology and size of gold nanocrystals [29]. Because different Miller-index surfaces of gold nanocrystals have a different adsorption capacity towards X^-, different crystal facets show a different growth rate. This leads to the formation of different gold nanocrystals with different morphologies [30]. Further research reveals that Cl^-, Br^-, and I^- play different roles in the shape-controlled synthesis of gold nanocrystals [31]. To achieve the synergy of Cl^-, Br^-, I^-, and CTA^+ in the shape control, the mixture of CTAC, KBr, and KI was employed for the shape-controlled synthesis of TO-Au. As shown in Fig. s1, the resulting TO-Au displays trisoctahedron nanostructures with uniform morphology and a large side length of 125 nm. In this step, X^- also can react with Au^{3+} to form the AuX_4^- complex. This decreases reduction potential of Au^{3+} and leads to a faster reduction of Au^{3+}. As AuI_4^- has a lower reduction potential compared with $AuCl_4^-$ and $AuBr_4^-$, the introduction

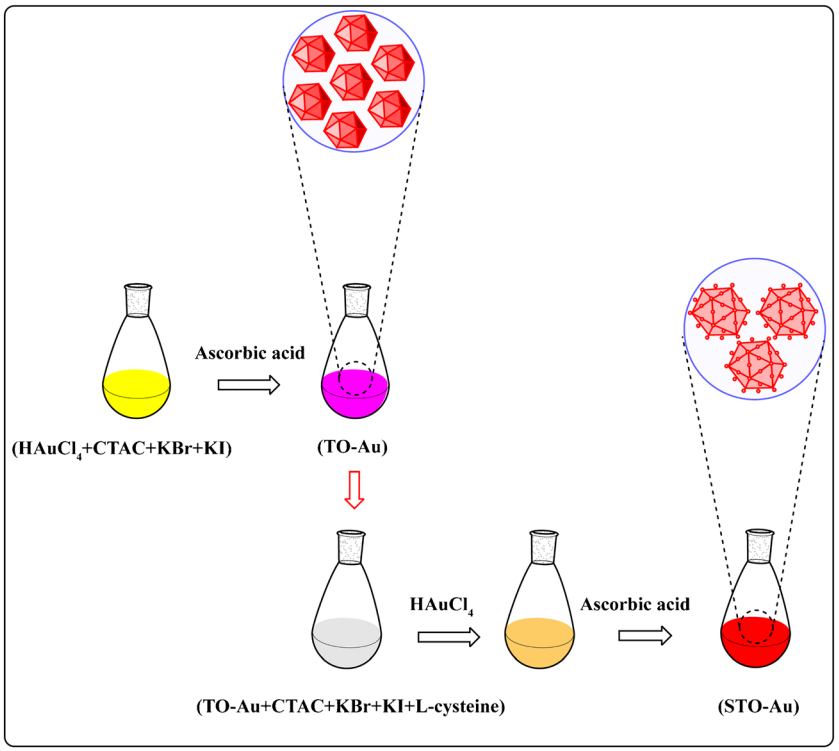

Fig. 1 Scheme for synthesis of STO-Au

of KI can accelerate the reduction of Au^{3+} and subsequent crystal growth. As a result, the synthesis of TO-Au can complete in a low temperature of 20 °C and a short time of 30 min.

The second step is the shape-controlled growth of TO-Au in the presence of CTAC, KBr, KI, and L-cysteine. In this step, the same mixed medium composing of CTAC, KBr, and KI for the preparation of TO-Au was used to keep the trisoctahedron nanostructure of gold nanocrystals. L-Cysteine as the chiral shape inducer was used for fabricating spiny gold shell. The Au-S bonding and other interactions between the functional groups in L-cysteine molecule and Au^{+} are involved in the shape-controlled growth of TO-Au. As the interaction between L-cysteine and gold nanocrystals offers high enantioselectivity, the enantioselective interactions at the interface between L-cysteine and gold nanocrystals result in an asymmetric evolution of TO-Au [32]. In addition, KI can also accelerate the growth of gold nanocrystals and structural evolution. Thus, the synthesis of STO-Au only requires the growth of 3 min at 20 °C.

Structural characterization

Figure 2 shows SEM, TEM, and HRTEM images and elemental mappings of the as-synthesized STO-Au. The results of the SEM and TEM analysis indicate that STO-Au has spiny trisoctahedral nanostructures with an average side length of 225 nm. The formation of such a structure is due to the special synthesis strategy of STO-Au. On the one hand, the shape induction of CTAC, KBr, and KI makes trisoctahedron gold nanocrystals with the side length of 200 nm. On the other hand, the enantioselective-directed growth of L-cysteine creates spiny gold nanocrystals with the particle size of 25 nm. The synergy of the above functions achieves to trisoctahedron gold@spiny gold core-shell structures with good monodispersity and more exposed high-index facets. In the structure, large gold nanocrystals as the core increase the electrical conductivity. Small spiny gold nanocrystals as the shell give large specific surface and highly exposed high-index facets. The former helps to improve the contacts between electrolyte and redox molecules. The latter brings a better catalytic activity. The integration of large gold core with small gold shell creates an outstanding catalytic behavior [33]. On the HRTEM image, there is an interplanar spacing of 0.18 nm, corresponding to the (111) plane of Au nanocrystal. The elemental mappings indicate the spatial distributions of Au, S, and I elements in the STO-Au. All elements show uniform distribution, verifying that these elements were involved in the formation and growth of gold nanocrystals. Further, EDS analysis was used to determine the element composition of STO-Au (Fig. s2; Table s2). The atomic percentages of Au, Cl, Br, I, and S are 94.28, 1.93, 1.4, 0.13, and 2.27, respectively. As S element only comes from L-cysteine, a high S context proves a strong affinity between gold nanocrystal and L-cysteine molecule during the gold crystal growth process.

Figure 3 shows the XRD patterns of STO-Au, TO-Au, and S-Au. On the XRD pattern of each gold nanocrystal, there are eight XRD diffraction peaks at 38.18°, 44.39°, 64.57°, 77.55°,

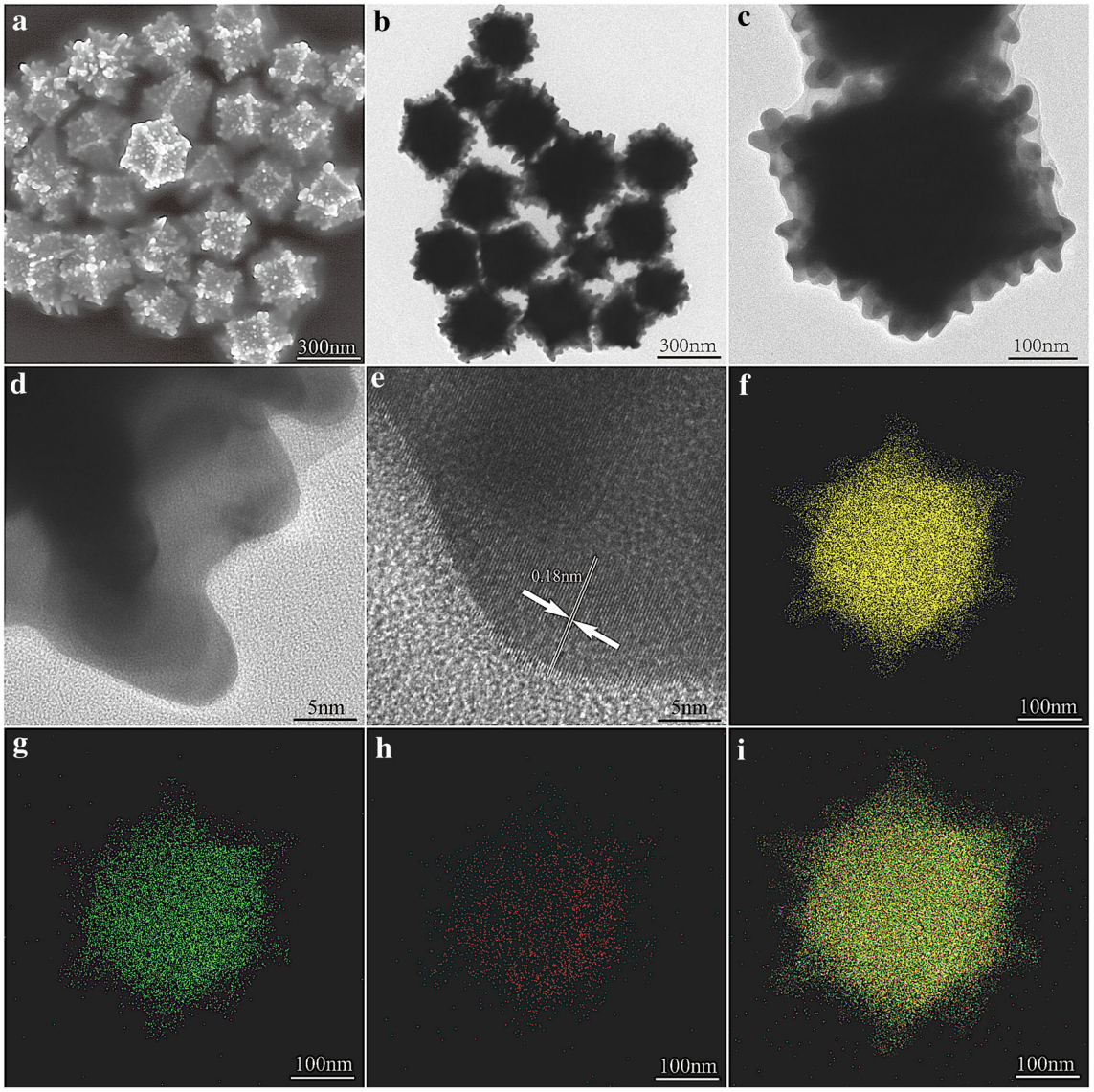

Fig. 2 SEM (**a**), TEM (**b**–**d**), HRTEM (**e**), and elemental mappings of Au (**f**), S (**g**), I (**h**), and EDS layered image (**i**) of STO-Au

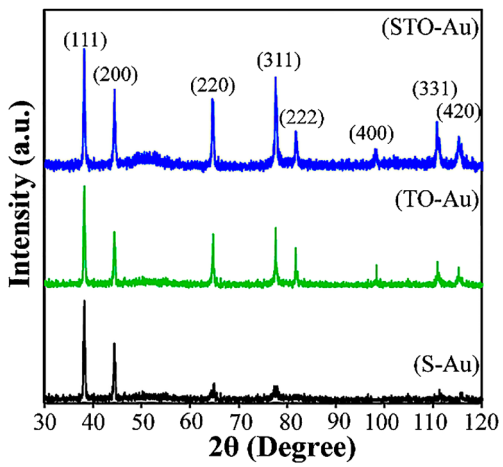

Fig. 3 XRD patterns of STO-Au, TO-Au, and S-Au

81.72°, 98.13°, 110.80°, and 115.26°, corresponding to the (111), (200), (220), (311), (222), (400), (311), and (420) faces of fcc gold nanocrystals. As all XRD patterns are well matched with those of fcc gold (JCPDS 4-0784), the above result demonstrates that the reduction of $HAuCl_4$ with ascorbic acid can form the fcc gold nanocrystals in the absence and the presence of shape inducers. However, STO-Au, TO-Au, and S-Au display a significant difference in the XRD diffraction intensity of high-index facets. In the absence of shape inducer, the reduction of $HAuCl_4$ with ascorbic acid forms spherical gold nanoparticles (S-Au). Among STO-Au, TO-Au, and S-Au, the high-index facet of S-Au offers the weakest XRD diffraction intensity, such as the (311), (222), (400), (311), or (420) facets. This is because in the absence of shape inducer the growth of low-index (111) and (200) facets is much faster than that of high-index (311), (222), (400),

(311), and (420) facets. With the reduction of Au^{+}, high-index facets are rapidly enclosed by low-index facets during the crystal growth process. This leads to the formation of spherical gold nanoparticles. The TO-Au has more exposed (311), (222), (400), (311), and (420) facets compared with S-Au. This is attributed to the shape induction of CTAC, KBr, and KI. In the presence of CTA^{+}, KBr, and KI, Cl^{-}, Br^{-}, and I^{-} can selectively adsorb on the different crystal facets. This adsorption increases the free energy of crystal facets and leads to a reduced growth rate. More importantly, the selective adsorption on the different crystal facets will reduce the difference in the growth rates between the low-index facets and high-index facets of gold nanocrystals. As a result, the resulting gold nanocrystals exhibit more exposed high-index crystal facets when a relatively short growth process was adopted for the synthesis. The STO-Au gives the highest XRD diffraction intensity of high-index facets. The XRD diffraction intensity of (331) facet is more than 3.7-fold that of TO-Au. This is mainly due to the asymmetric evolution of gold nanocrystals caused by L-cysteine. The more exposure of high-index facets leads to an improved catalytic activity of gold nanocrystals, which has been demonstrated by the results of SERS analysis (Fig. s3).

Sensing principle

Thi-STO-Au-P1 and Thi-STO-Au-P2 were designed as the redox probes for the construction of electrochemical sensing platform for the detection of MON89788 gene (Fig. 4). Firstly, hairpin DNA 1 (H1), Thi-STO-Au-P1, and Thi-STO-Au-P2 self-assemble into the two-dimensional DNA nanopores (DNPs) on the surface of MCH/S1-S2/GE. The formation of DNPs leads to the immobilization of Thi-STO-Au-P1 and Thi-STO-Au-P2 on the electrode surface. The oxidation and reduction of Thi molecules under the in situ catalysis of STO-Au produce a sensitive electrochemical response. Then, target DNA hybridizes with hairpin DNA 2 (H2) by base pairing to open hairpin structure of H2. The opened H2 will bind with H1 in DNPs, leading to the collapse of DNPs. The collapse of one DNP removes two redox probes from the electrode surface and brings a reduced electrochemical response. With the collapse of DNP, target DNA is released from Target-H2 hybrid. The released target DNA uses to open another H2, triggering the next target DNA recycling. By target DNA recycling, one target DNA can remove 2N redox probes from the electrode surface. This produces significant signal amplification. The signal amplification will be further improved by STO-Au. Large size and high chemical activity make one STO-Au bind thionine molecules ($n > 1$). In situ catalysis of STO-Au towards redox of thionine increases the electrochemical response. The above factors greatly improve the sensitivity for the detection of MON89788 gene.

To prove the feasibility of the proposed sensing platform for the detection of MON89788, the CV and EIS behaviors of different electrodes were investigated in 1 mM $Fe(CN)_6^{4-}$. Figure 5a and b indicate that the S1-S2/GE has a lower CV current density and a higher electron transfer impedance (R_{ct}) compared with the bare GE. The immobilization of S1 and S2 partly blocks the channels for the electron transfer between electrode and electrolyte, leading to a reduced CV current density and an increased R_{ct}. When modified with MCH, the CV current density further decreases with increasing R_{ct}. This is because the modification of MCH on the electrode surface blocks more channels for the electron transfer. However,

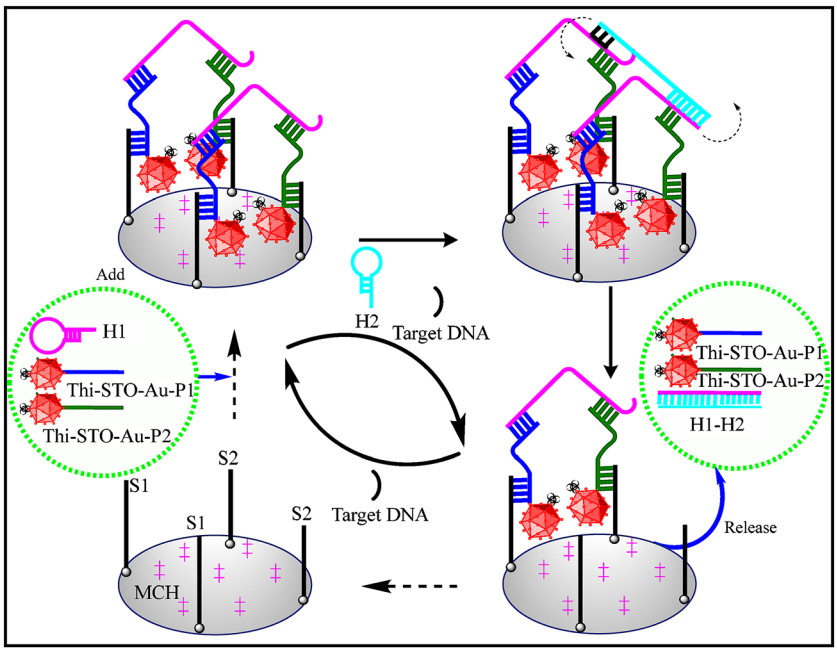

Fig. 4 Illustration of electrochemical sensing platform for detection of MON89788

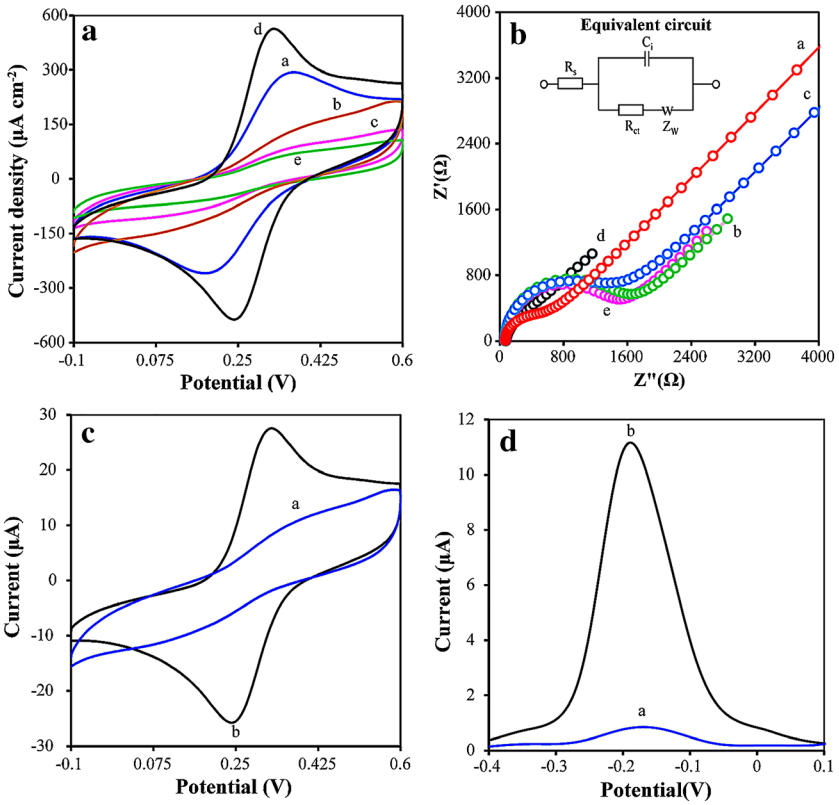

Fig. 5 CV (**a**) and EIS curves (**b**) of bare GE (a), S1-S2/GE (b), MCH/S1-S2/GE (c), and DNP/MCH/S1-S2/GE incubated in 2 μM H2 solution with (d) and without (e) 2 fM target DNA in 1.0 mM $Fe(CN)_6^{4-}$. The CV curves (**c**) at 50 mV s^{-1} and DPV curves (**d**) of DNP/MCH/S1-S2/GE incubated in 2 μM H2 solution with (a) and without (b) 2 fM target DNA in the PBS of pH 7.4

DNPs/MCH/S1-S2/GE displays the highest CV current density and the smallest R_{ct}. Due to high electrical conductivity and catalytic activity, the STO-Au accelerates the redox of $Fe(CN)_6^{4-}$ on the electrode surface. This leads to an increased CV current density and a reduced R_{ct}. The result also verifies the formation of DNPs on the electrode surface. When the electrode was incubated in the mixed H2 solution containing target DNA (MON89788), the CV current density obviously decreases with increasing R_{ct}. In the presence of target DNA, the incubation results in the removal of redox probes from the electrode surface. This brings a reduction in the CV current density and increase in the R_{ct}, because of the decrease of electrical conductivity. The result also demonstrates that the target-induced signal amplification was triggered in the presence of target DNA. The change in the electrochemical signal before and after the incubation can be used for the detection of MON89788.

Electrochemical response to MON89788

The CV and DPV behaviors of DNP/MCH/S1-S2/GE incubated in the H2 solution with and without target DNA were studied in the PBS of pH 7.4. Figure 5c and d indicate that the incubation cannot cause obvious change in the CV and DPV currents in the absence of target DNA. Because the base sequences that can hybridize with H1 are embedded in the hairpin structure of H2, H2 cannot bind with H1 in the DNPs to release the redox probes from the electrode surface. As a result, no obvious change in the CV and DPV currents can occur in the incubation. However, the incubation produces an obvious reduce in the CV and DPV currents in the presence of target DNA. This is because in the presence of target DNA MON89788 hybridizes with H2 to open the hairpin structure of H2. The opened H2 binds with H1 and leads to collapse of DNPs. With the collapse of DNPs, many redox probes were released from the electrode surface. This produces an obvious decrease in the CV and DPV current, because of reducing number of redox probes on the electrode surface. The change in CV or DPV signal caused by the incubation can be used for electrochemical detection of MON89788. Compared with the CV measurement, the DPV technique has a more sensitive electrochemical response to the same concentration of MON89788. Therefore, the DPV technique was employed for the electrochemical detection of MON89788.

In one detection, only a small part of DNPs were collapsed on the electrode surface; thus, the proposed biosensor can be directly used for the next detection of MON89788 after the detection was completed. To evaluate the reusability of the biosensor, the biosensor was repeatedly used to measure 2.0 fM target DNA by using the same procedure. Figure s4 presents change in the DPV peak current caused by 2.0 fM target DNA (ΔI_p) at different detection times. Each of the detections produces a similar ΔI_p when the detection time is less than 220, indicating a good reusability.

Analytical characteristics

The conditions for construction of DNPs and detection of MON89788 were optimized and the results are shown in Fig. s5–9. The optimized conditions were 1 μM of the redox probe and 120 min of incubation time at 37 °C for the construction of DNPs and 120 min of incubation time at 37 °C for the detection of MON89788.

To prove the practicability for the detection of MON89788, DNP/MCH/S1-S2/GE was incubated in 2×10^{-6} M of the annealed H2 solution containing different concentrations of target DNA and its DPV curves were measured in the PBS under the optimized conditions. Figure 6a shows that the DPV current reduces with increasing target DNA. At a higher concentration of target DNA, more redox probes were removed from the electrode surface due to faster target DNA recycling reaction. This leads to a reduction in DPV current. Further, Fig. 6b indicates a linear dependence with the logarithm of MON89788 concentration in the range of 0.02–8×10^4 fM. The linear regression equation is I_p(μA) at − 0.18 V vs. Ag/AgCl = − 2.2687 × Log[$C_{\text{target DNA}}$, fM] + 14.489, with a correlation coefficient (R^2) of 0.994. The detection limit (LOD) is 0.0048 fM for the detection of MON89788 (S/N = 3), indicating a high sensitivity. The sensor was stored at 4 °C. Then, it is taken out every other week and used for the detection of 1.0 fM MON89788 gene. Two months of storage only causes 5% change in DPV peak current, verifying good stability.

To assess the contribution of STO-Au towards sensitivity, another electrochemical sensing platform was constructed and its analytical parameters for MON89788 were measured by the same procedure except for S-Au instead of STO-Au in redox probes. The linear range and LOD are 3.5–9×10^6 fM and 1.8 fM, respectively. The data indicates that the sensitivity of biosensors with STO-Au is more than 375-fold that of biosensor with S-Au. The improved sensitivity is attributed to special structure of STO-Au. Large size and more exposed high-index facets of STO-Au greatly enhance the catalytic activity of gold nanocrystals. This helps to improve the sensitivity for electrochemical detection of MON89788.

DPV response in single-base mismatched MON89788 (S-DNA), two-base mismatched MON89788 (T-DNA), and non-complementary MON89788 (N-DNA) was investigated to evaluate the specificity of proposed biosensor. Figure s10 shows that only T-DNA causes obvious reduction in DPV peak current. S-DNA, T-DNA, and N-DNA lead to small decrease in DPV peak current. The peak current in S-DNA, T-DNA, or N-DNA is close to that in blank solution. This is due to incomplete complementary between base pairs. S-DNA, T-DNA, or N-DNA cannot hybridize with H2 to open hairpin structure of H2. Thus, H2 does not bind with H1 and triggers the target DNA recycling. As no redox probes were removed from the electrode surface, the DPV response still tends to stable. The results verify that the proposed biosensor has good specificity for MON89788.

Comparison with other methods

For the sake of comparison, analytical parameters of different electrochemical sensors for detection of DNA are listed in Table 1. Firstly, the proposed biosensor gives the highest sensitivity, which is much better than that of other methods. This is mainly attributed to the use of STO-Au for target DNA recycling amplification. Due to high catalytic activity, the catalytic effect of STO-Au on the redox of Thi will significantly improve the response towards DNA. This achieves to ultrasensitive detection of MON89788. Secondly, the special design of target DNA–induced recycling amplification brings a high specificity. Only target DNA can trigger the recycle reaction and produces a sensitive electrochemical signal. This achieves high selectivity for detection of MON89788. Thirdly, the proposed biosensor offers a good repeatability. This is due to no use of any biological enzymes. This avoids the problems caused by the instability of biological enzymes and leads to high stability and repeatability for detection of DNA. However, the proposed method took some more time for detection of DNA and there is still something for improvement in the future.

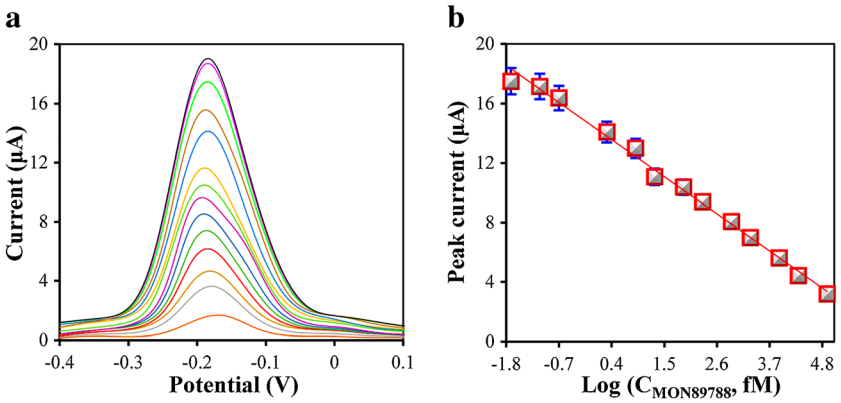

Fig. 6 **a** DPV curves of DNP/MCH/S1-S2/GE incubated in 0.0, 0.02, 0.08, 0.2, 2, 8, 20, 30, 200, 800, 2000, 8000, 20,000, 80,000, and 100,000 fM target DNA in the PBS of pH 7.4 (from bottom to top). **b** The relationship curve of DPV peak current at − 0.18 V vs. Ag/AgCl (I_p) with the logarithm of target DNA concentration

Table 1 Analytical parameters of different electrochemical sensors for detection of DNA

Sensing material	Detection technique	DNA species	Linear range (fM)	Detection limit (fM)	Ref.
Fe_3O_4@Au	Chronocoulometry	Gene sequence of transgenic soybean	0.1–0.01	0.045	[17]
Graphene and TiO_2	Differential pulse voltammetry	MON89788	1×10^3–1×10^9	721	[25]
Au	Differential pulse voltammetry	DNA methylation	10–10×10^5	4	[34]
Doxorubicin-Au	Differential pulse voltammetry	Circulating tumor DNA	0.1–1×10^8	0.29	[35]
LAMP-H^+-Au	Square wave voltammetry	Flu A virus biomarker DNA	0.1–1×10^8	0.018	[36]
AgDNCs-DNA-AgNCs	Differential pulse voltammetry	EBV-related DNA	1–1×10^6	0.38	[37]
Tetrahedral DNA nanostructures and G-quadruplex–hemin	Differential pulse voltammetry	MicroRNA-21	0.1–100	0.04	[38]
Cross-shaped DNA origami	Differential pulse voltammetry	MicroRNA	1×10^2–1×10^7	79.8	[39]
Au-MOF-5	Differential pulse voltammetry	DNA	1×10^5–1×10^8	50	[40]
Polyaniline-graphene	Differential pulse voltammetry	HIV DNA	0.5–1.0 × 105	0.1	[41]
Ferrocene-poly(amidoamine)	Differential pulse voltammetry	Breast cancer gene	1.3×10^6–2×10^7	3.8×10^5	[42]
STO-Au	Differential pulse voltammetry	MON89788	0.02–8×10^4	0.0048	Present work

Sample analysis

The as-proposed biosensor was applied in electrochemical detection of MON89788 gene sequences in PCR products from genetically modified soybean and non-genetically modified soybean. The recovery experiment was carried out by adding known concentration of target DNA into PCR product from non-genetically modified soybean sample. The spiked concentration of MON89788 gene was based on the information with experimental evidences [17]. Table 2 indicates that the recovery is in the range of 96.4–105% and RSD ($n = 5$) is between 2.3 and 4.2%, verifying that the biosensor has good recovery and applicability. The DPV curves of the proposed biosensor incubated in the H2 solution in the absence (blank) and the presence of PCR products from the non-genetically modified soybean (non-GM) and genetically modified soybean (GM) were measured. Figure s11 indicates that the incubation in the non-GM only brings very low change in DPV response. However, the incubation in GM produces obvious decrease in DPV response. The significant difference of DPV signals between non-GM and GM verifies that the proposed biosensor can effectively detect the PCR product of soybean samples.

Conclusions

We have demonstrated the synthesis of spiny trisoctahedron gold nanocrystal and its use for construction of electrochemical MON89788 gene biosensor. The sensitivity of DNA biosensor was greatly improved due to double signal amplification of spiny trisoctahedron gold nanocrystal and target DNA–induced recycling reaction. The detection limit of target DNA was obtained at 0.0048 fM. The technique has been successfully applied in soybean sample detection, and it provides a promising electrochemical platform for detection of DNA in disease diagnosis, food safety, biological identification, and archeology.

Table 2 The results for electrochemical detection of MON89788 sequence in PCR products from soybean samples ($N = 5$)

Samples	Target DNA added (fM)	MON89788 gene fragments found by the proposed method (fM)	Recovery (%)
1#	0.0	No found	
	100.0	98.3 ± 1.8	98.3
2#	0.0	No found	
	500.0	511.3 ± 6.2	102
3#	0.0	No found	
	1000.0	977.0 ± 4.7	97.7
4#	0.0	No found	
	1000	1050.2 ± 8.9	105
5#	0.0	No found	
	5000	4820.4 ± 12.6	96.4

Funding information This study was financially supported by the National Key Research and Development Program of China (No. 2018YFC1603001), National Natural Science Foundation of China (No. 21576115), and Science Foundation of Jiangsu Province Special Equipment Safety Supervision Inspection Institute (KJ(Y) 2017014).

Compliance with ethical standards

Conflict of interest The author(s) declare that they have no competing interests.

References

1. Oreskovic A, Panpradist N, Marangu D, Brault ND, Lai JJ, Horner DJ, Lutz BR (2019) Sensitive hybridization capture and detection of urine cell-free DNA for tuberculosis diagnosis. J Mol Diagn 21: 1164–1165. https://doi.org/10.1016/S1525-1578(19)30391-5
2. Maralit BA, Aguila RD, Ventolero MFH, Perez SKL, Willette DA, Santos MD (2013) Detection of mislabeled commercial fishery by-products in the Philippines using DNA barcodes and its implications to food traceability and safety. Food Control 33:119–125. https://doi.org/10.1016/j.foodcont.2013.02.018
3. Lewis CA, Layne TR, Seashols-Williams SJ (2019) Detection of microRNAs in DNA extractions for forensic biological source identification. J Forensic Sci 64:1823–1830. https://doi.org/10.1111/1556-4029.14070
4. West C, Hofman CA, Ebbert S, Martin J, Shirazi S, Dunning S, Maldonado JE (2017) Integrating archaeology and ancient DNA analysis to address invasive species colonization in the Gulf of Alaska. Conserv Biol 31:1163–1172. https://doi.org/10.1111/cobi.12865
5. Liu X, Zhou X, Xia X, Xiang H (2020) Catalytic hairpin assembly-based double-end DNAzyme cascade-feedback amplification for sensitive fluorescence detection of HIV-1 DNA. Anal Chim Acta 1096:159–165. https://doi.org/10.1016/j.aca.2019.10.051
6. Wei Q, Liu X, DeFrank G, Yemelyanova A, Harada S (2019) Validation of extracted DNA for detection of KRAS mutations with Idylla PCR-based molecular diagnostic assay: can we rescue small samples? J Mol Diagn 21:1200–1249. https://doi.org/10.1016/S1525-1578(19)30391-5
7. Fu XL, Wen JH, Li JW, Lin H, Liu YM, Zhuang XM, Tian CY, Chen LX (2019) Highly sensitive detection of prostate cancer specific PCA3 mimic DNA using SERS-based competitive lateral flow assay. Nanoscale 11:15530–15536. https://doi.org/10.1039/C9NR04864B
8. Kaygusuz D, Vural S, Aytekin AO, Lucas SJ, Elitas M (2019) DaimonDNA: a portable, low-cost loop-mediated isothermal amplification T platform for naked-eye detection of genetically modified organisms in resource-limited settings. Biosens Bioelectron 141:111409. https://doi.org/10.1016/j.bios.2019.111409
9. Mills DM, Foguel MV, Martin CP, Trieu TT, Kamar O, Calvomarzal P, Kolpashchikov DM, Chumbimuntiorres KY (2019) Rapid detection of different DNA analytes using a single electrochemical sensor. Sens Actuators B Chem 293:11–15. https://doi.org/10.1061/j.snb.2019.04.149
10. Kuzin Y, Kappo D, Porfireva A, Shurpik D, Stoikov I, Evtugyn G, Hianik T (2018) Electrochemical DNA sensor based on carbon blackpoly(neutral red) composite for detection of oxidative DNA damage. Sensors 18:14. https://doi.org/10.3390/s18103489
11. Jin X, Zhou L, Zhu B, Jiang X, Zhu NN (2018) Silver-dendrimer nanocomposites as oligonucleotide labels for electrochemical stripping detection of DNA hybridization. Biosens Bioelectron 107: 237–243. https://doi.org/10.1016/j.bios.2018.02.033
12. Mogha NK, Sahu V, Sharma RK, Masram DT (2018) Reduced graphene oxide nanoribbon immobilized gold nanoparticle based electrochemical DNA biosensor for the detection of Mycobacterium tuberculosis. J Mat Chem B 6:5181–5187. https://doi.org/10.1039/C8TB01604F
13. Wang ZF, Yang JJ, Jiang YY, Zhang YY, Zhang LM, Wu FG, He N (2015) Electrochemical detection of DNA by using "Pd/GO label copper stain" for signal amplification. Anal Methods 7:8554–8560. https://doi.org/10.1039/C5AY02369F
14. Wu F, Lin Q, Wang LL, Zou YL, Chen M, Xia YK, Lan JM, Chen JH (2020) A DNA electrochemical biosensor based on triplex DNA-templated Ag/Pt nanoclusters for the detection of single-nucleotide variant. Talanta 207:7. https://doi.org/10.1016/j.talanta.2019.120257
15. Gao HW, Sun M, Lin C, Wang SB (2012) Electrochemical DNA biosensor based on graphene and TiO_2 nanorods composite film for the detection of transgenic soybean gene sequence of MON89788. Electroanal 24:2283–2290. https://doi.org/10.1002/elan.201200403
16. Pinijsuwan S, Rijiravanich P, Somasundrum M, Surareungchai W (2010) Attomolar electrochemical detection of DNA hybridization based on enhanced latex/gold nanoparticles. Adv Eng Mater 12: B649–B653. https://doi.org/10.1002/adem.201080039
17. Chen DL, Zhang M, Ma MY, Hai H, Li JP, Shan Y (2019) A novel electrochemical DNA biosensor for transgenic soybean detection based on triple signal amplification. Anal Chim Acta 1078:24–31. https://doi.org/10.1016/j.aca.2019.05.074
18. Shah KW, Zheng L (2019) Microwave-assisted synthesis of hexagonal gold nanoparticles reduced by organosilane (3-mercaptopropyl) trimethoxysilane. Materials 12:11. https://doi.org/10.3390/ma12101680
19. Taj A, Shaheen A, Xu J, Estrela P, Mujahid A, Asim T, Iqbal MZ, Khan WS, Bajwa SZ (2019) In-situ synthesis of 3D ultrasmall gold augmented graphene hybrid for highly sensitive electrochemical binding capability. J Colloid Interf Sci 553:289–297. https://doi.org/10.1016/j.jcis.2019.06.013
20. Qin YZ, Lu YX, Pan WF, Yu DD, Zhou JG (2019) One-pot synthesis of hollow hydrangea Au nanoparticles as a dual catalyst with SERS activity for in situ monitoring of a reduction reaction. RSC Adv 9:10314–10319. https://doi.org/10.1039/C9RA00733D
21. Piella J, Gonzalez-Febles A, Patarroyo J, Arbiol J, Bastus NG, Puntes V (2019) Seeded-growth aqueous synthesis of colloidal-stable citrate-stabilized Au/CeO_2 hybrid nanocrystals: heterodimers, core@shell, and clover- and star-like structures. Chem Mater 31:7922–7932. https://doi.org/10.1021/acs.chemmater.9b02005
22. Li RY, Yang TT, Li ZJ, Gu ZG, Wang GL, Liu JK (2017) Synthesis of palladium@gold nanoalloys/nitrogen and sulphur-functionalized multiple graphene aerogel for electrochemical detection of dopamine. Anal Chim Acta 954:43–51. https://doi.org/10.1016/j.aca.2016.12.031
23. Chuang YC, Hsia Y, Chu CH, Lin LJ, Sivasubramanian M, Lo LW (2019) Precision control of the large-scale green synthesis of biodegradable gold nanodandelions as potential radiotheranostics. Biomater Sci 7:4720–4729. https://doi.org/10.1039/C9BM00897G
24. Qin YZ, Lu YX, Yu DD, Zhou JG (2019) Controllable synthesis of au nanocrystals with systematic shape evolution from an octahedron to a truncated ditetragonal prism and rhombic dodecahedron. Crystengcomm 21:5602–5609. https://doi.org/10.1039/C9CE01022J
25. Ma YY, Kuang Q, Jiang ZY, Xie ZX, Huang RB, Zheng LS (2008) Synthesis of trisoctahedral gold nanocrystals with exposed high-index facets by a facile chemical method. Angew Chem Int Edit 47:8901–8904. https://doi.org/10.1002/anie.200802750
26. Li RY, Li ZJ, Sun XL, Jin J, Liu L, Gu ZG, Wang GL (2020) Graphene quantum dot-rare earth upconversion nanocages with

extremely high efficiency of upconversion luminescence, stability and drug loading towards controlled delivery and cancer theranostics. Chem Eng J 382:122992. https://doi.org/10.1016/j.cej.2019.122992

27. Li RY, Zhu HY, Li ZJ, Liu JK (2018) Electrochemical determination of acetaminophen using a glassy carbon electrode modified with a hybrid material consisting of graphene aerogel and octadecylamine-functionalized carbon quantum dots. Microchim Acta 185:9. https://doi.org/10.1007/s00604-018-2688-7
28. Ahn HY, Lee HE, Jin K, Nam KT (2013) Extended gold nanomorphology diagram: synthesis of rhombic dodecahedra using CTAB and ascorbic acid. J Mater Chem C 1:6861–6868. https://doi.org/10.1039/C3TC31135J
29. Sun MJ, Ran GJ, Fu Q, Xu WL (2015) The effect of iodide on the synthesis of gold nanoprisms. J Exp Nanosci 10:1309–1318. https://doi.org/10.1080/17458080.2014.1003340
30. Wei L, Sheng T, Ye JY, Lu BA, Tian N, Zhou ZY, Zhao XS, Sun SG (2017) Seeds and potentials mediated synthesis of high-index faceted gold nanocrystals with enhanced electrocatalytic activities. Langmuir 33:6991–6998. https://doi.org/10.1021/acs.langmuir.7b00964
31. Li LD, Peng Y, Yue YH, Hu Y, Liang X, Yin PG, Guo L (2015) Synthesis of concave gold nanocuboids with high-index facets and their enhanced catalytic activity. Chem Commun 51:11591–11594. https://doi.org/10.1039/C5CC02106E
32. Lee HE, Ahn HY, Mun J, Lee YY, Kim M, Cho HN, Chang K, Kim WS, Rho J, Nam KT (2018) Amino-acid- and peptide directed synthesis of chiral plasmonic gold nanoparticles. Nature 556:360–365 https://doi.org/10.1038/s41586-018-0034-1
33. Zhang XL, Yang ZH, Chang YY, Qing M, Yuan R, Chai YQ (2018) Novel 2D-DNA-nanoprobemediated enzyme-free-target-recycling amplification for the ultrasensitive electrochemical detection of microRNA. Anal Chem 90:9538–9544. https://doi.org/10.1021/acs.analchem.8b02251
34. Feng QM, Qin L, Wang MY, Wang P (2020) Signal-on electrochemical detection of DNA methylation based on the target-induced conformational change of a DNA probe and exonuclease III-assisted target recycling. Biosens Bioelectron 149:111847. https://doi.org/10.1016/j.bios.2019.111847
35. Li DD, Xu YX, Fan L, Shen B, Ding XJ, Yuan R, Li XM, Chen WX (2020) Target-driven rolling walker based electrochemical biosensor for ultrasensitive detection of circulating tumor DNA using doxorubicin@tetrahedron-Au tags. Biosens Bioelectron 148:111826. https://doi.org/10.1016/j.bios.2019.111826
36. Hua XY, Yang EF, Yang WT, Yuan R, Xu WJ (2019) LAMP-generated H^+ ions-induced dimer i-motif as signal transducer for ultrasensitive electrochemical detection of DNA. Chem Commun 55:12463–12466. https://doi.org/10.1039/C9CC06738H
37. Que HY, Zhang DC, Guo B, Wang T, Wu HP, Han DB, Yan YR (2019) Label-free and ultrasensitive electrochemical biosensor for the detection of EBV-related DNA based on AgDNCs@DNA/AgNCs nanocomposites and lambda exonuclease-assisted target recycling. Biosens Bioelectron 143:111610. https://doi.org/10.1016/j.bios.2019.111610
38. Lu J, Wang J, Hu XL, Gyimah E, Yakubu S, Wang K, Wu XY, Zhang Z (2019) Electrochemical biosensor based on tetrahedral DNA nanostructures and G-quadruplex–hemin conformation for the ultrasensitive detection of microRNA-21 in serum. Anal Chem 91:7353–7359. https://doi.org/10.1021/acs.analchem.9b01133
39. Han S, Liu WY, Yang S, Wang RS (2019) Facile and label-free electrochemical biosensors for microRNA detection based on DNA origami nanostructures. ACS Omega 4:11025–11031. https://doi.org/10.1021/acsomega.9b01166
40. Yang HM, Han LJ, Liu J, Li YP, Zhang DD, Liu X, Liang ZH (2019) Highly sensitive electrochemical biosensor assembled by Au nanoparticle /MOF-5 composite electrode for DNA detection. Int J Electrochem Sci 14:5491–5507. https://doi.org/10.20964/2019.06.49
41. Gong QJ, Han HX, Yang HY, Zhang ML, Sun XL, Liang YX, Liu ZR, Zhang WC, Qiao JL (2019) Sensitive electrochemical DNA sensor for the detection of HIV based on a polyaniline/graphene nanocomposite. J Mater 5:313–319. https://doi.org/10.1016/j.jmat.2019.03.004
42. Senel M, Dervisevic M, Kokkokoglu F (2019) Electrochemical DNA biosensors for label-free breast cancer gene marker detection. Anal Bioanal Chem 411:2925–2935. https://doi.org/10.1007/s00216-019-01739-9